

CHEMISTRY

A **European** Journal

Supporting Information

First-Principles Calculation, Synthesis, and Catalytic Properties of Rh-Cu Alloy Nanoparticles

Tokutaro Komatsu,^{*[a, b]} Hirokazu Kobayashi,^[a, c] Kohei Kusada,^[a] Yoshiki Kubota,^[d]
Masaki Takata,^[e, f] Tomokazu Yamamoto,^[g] Syo Matsumura,^[g] Katsutoshi Sato,^[h, i]
Katsutoshi Nagaoka,^[h, i] and Hiroshi Kitagawa^{*[a, j, k]}

chem_201604286_sm_miscellaneous_information.pdf

EXPERIMENTAL AND CALCULATION DETAILS

Identification

Transmission electron microscopy (TEM) images were recorded by using Hitachi HT7700 with acceleration voltage of 100 kV. Energy-dispersive x-ray spectroscopy (EDS) was measured with Bruker Quantax attached to HT7700. High-angle annular dark-field scanning transmission electron microscopy (HAADF-STEM) images and elemental mapping with EDS were obtained with JEOL JEM-ARM200F operated at 200 kV. Powder X-ray diffraction (PXRD) patterns for Rietveld refinement were measured at SPring-8 BL02B2 with X-ray wavelength ($\lambda = 0.58001, 0.58024 \text{ \AA}$) calibrated by the lattice constant of CeO_2 . High-temperature PXRD patterns were recorded on a sample sealed in a quartz capillary under vacuum. To check for crystalline impurity and phase separation, PXRD patterns for Le Bail fitting were recorded with Bruker D8 Advance.

Measurement of three-way catalytic activity

The synthesized $\text{Rh}_{1-x}\text{Cu}_x$ nanoparticles were supported on $\gamma\text{-Al}_2\text{O}_3$ catalysts by wet impregnation. The amount of nanoparticles was 1 wt% of $\gamma\text{-Al}_2\text{O}_3$. Three-way catalytic activity was measured between $T = 25 - 600 \text{ }^\circ\text{C}$ on a gas mixture of CO : 5046 ppm, O_2 : 4920 ppm, H_2 : 1758 ppm, CO_2 : 12.45 %, C_3H_6 : 467 ppm, NO : 1161 ppm and He balance at a total flow rate of 200 ml min^{-1} . The space velocity was set to $3 \times 10^5 \text{ ml g}^{-1} \text{ h}^{-1}$. The exit composition of the gases was continuously monitored with a chemiluminescence NO_x analyser and a non-dispersive infrared gas analyser (VA3000, HORIBA).

Band Calculation

Structural optimization based on band calculations were carried out using density functional theory (PBE functional^{S1}) implemented in CASTEP^{S2} in Materials Studio (Dassault Systèmes Biovia, Inc.). Plane-wave basis functions with a cut-off energy of 300 eV were used with ultrasoft pseudopotentials.^{S3} A k-point mesh of $3 \times 3 \times 3$ was sampled by the Monkhorst–Pack grid method.^{S4} The DOS and relative energy were calculated with norm-conserving pseudopotentials, basis-set cut-off of 880 eV, and a k-point mesh of $13 \times 13 \times 13$ sampled by the Monkhorst–Pack grid method. To count the PDOS, the first Brillouin zone was sampled at $13 \times 13 \times 13$ k points with interpolation. The $\text{DOS}(E_F)$ is defined as the averaged DOS within $\pm 0.1 \text{ eV}$ of E_F .

The calculation models were derived from $2 \times 2 \times 2$ supercell based on face-centred cubic lattice, thus contains 32 atoms. To maintain the cubic symmetry, the supercell was assumed to belong to space group $\text{Pm}\bar{3}\text{m}$. The symmetry-related sites are listed in Table S1. Due to the constraint by the symmetry, number of Cu atoms in the model is limited to 0-8, 12-20 and 24-32.

Table S1. Fractional coordinates of symmetry-related sites in $2 \times 2 \times 2$ supercell based on face-centred cubic lattice.

Site 1a (1 site)	Site 1b (1 site)	Site 2a (3 sites)	Site 2b (3 sites)	Site 3a (12 sites)	Site 3b (12 sites)
(0, 0, 0)	(0.5, 0.5, 0.5)	(0, 0.5, 0.5)	(0.5, 0, 0)	(0, 0.25, 0.25)	(0.5, 0.25, 0.25)
		(0.5, 0, 0.5)	(0, 0.5, 0)	(0.25, 0, 0.25)	(0.25, 0.5, 0.25)
		(0.5, 0.5, 0)	(0, 0, 0.5)	(0.25, 0.25, 0)	(0.25, 0.25, 0.5)
				(0, 0.75, 0.75)	(0.5, 0.75, 0.75)
				(0.75, 0, 0.75)	(0.75, 0.5, 0.75)
				(0.75, 0.75, 0)	(0.75, 0.75, 0.5)
				(0, 0.25, 0.75)	(0.5, 0.25, 0.75)
				(0.75, 0, 0.25)	(0.75, 0.5, 0.25)
				(0.25, 0.75, 0)	(0.25, 0.75, 0.5)
				(0, 0.75, 0.25)	(0.5, 0.75, 0.25)
				(0.25, 0, 0.75)	(0.25, 0.5, 0.75)
				(0.75, 0.25, 0)	(0.75, 0.25, 0.5)

RESULTS

Band Calculation

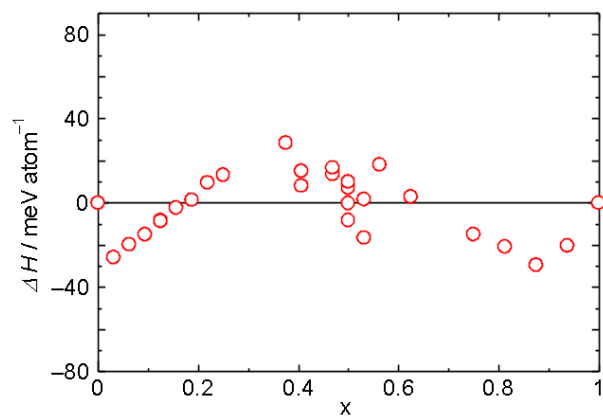


Figure S1. Formation enthalpy of $\text{Rh}_{1-x}\text{Cu}_x$ ordered alloy calculated with density-functional theory.

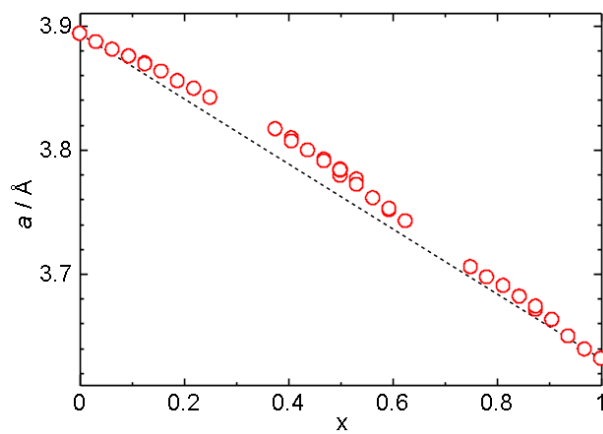


Figure S2. Lattice parameter of $\text{Rh}_{1-x}\text{Cu}_x$ ordered alloy calculated with density-functional theory.

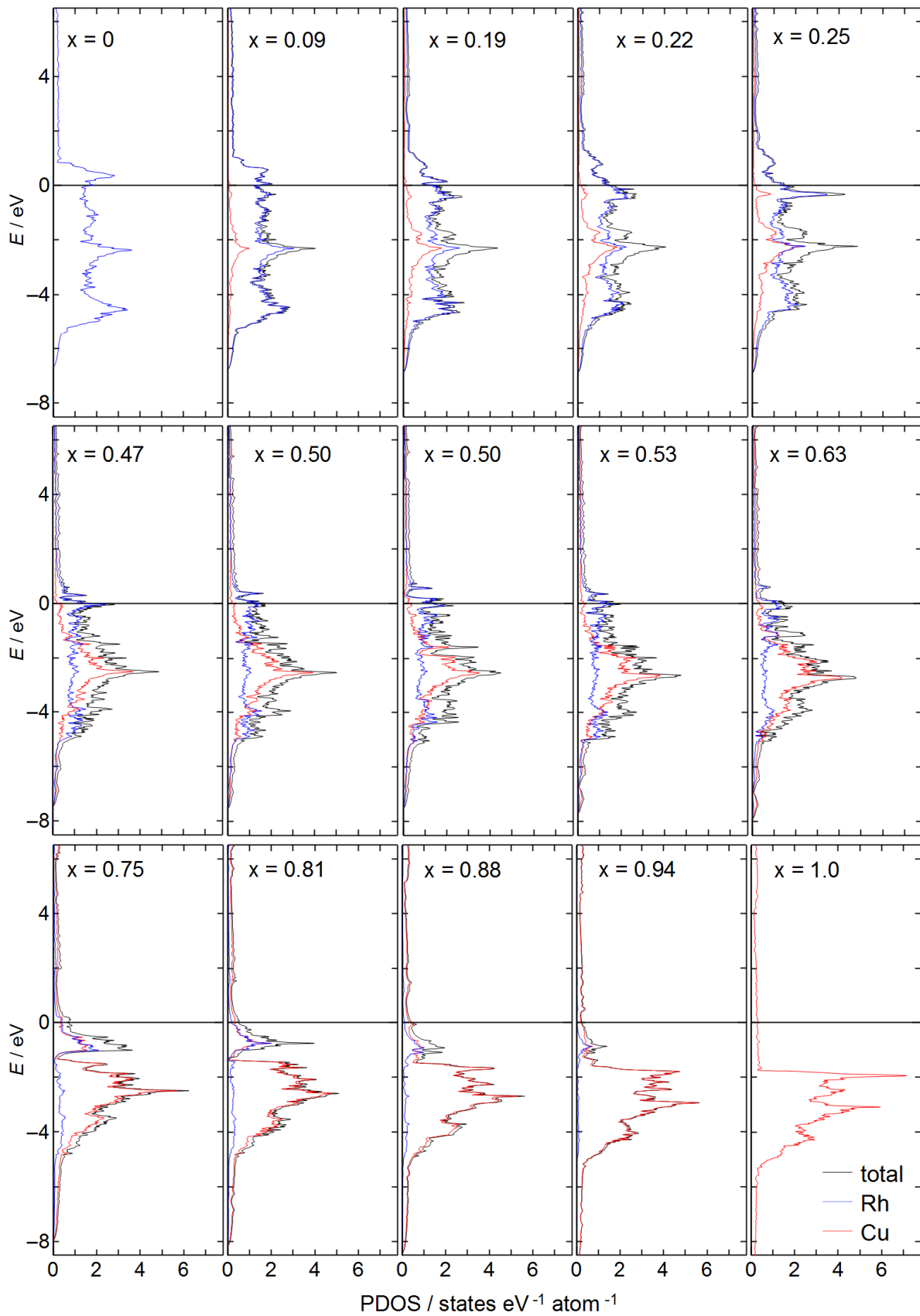


Figure S3. Calculated partial density of states (PDOS) of $\text{Rh}_{1-x}\text{Cu}_x$ ordered alloys.

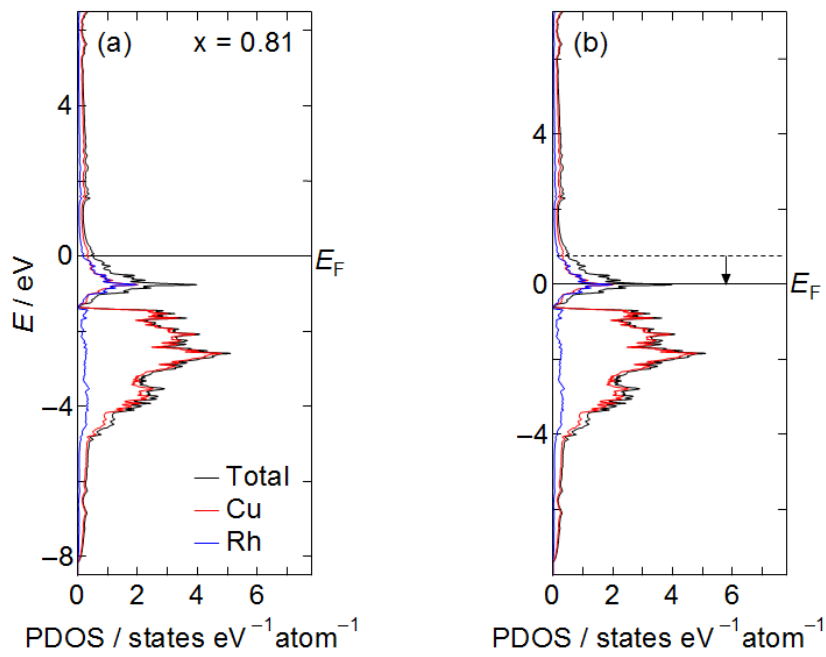


Figure S4. Calculated partial density of states (PDOS) of Cu-rich $\text{Rh}_{1-x}\text{Cu}_x$ ordered alloy (a). Removal of 0.8 electron per atom can lower the Fermi level (E_F) (b). The electron withdrawal would increase the $\text{DOS}(E_F)$ to ca. 4 states $\text{eV}^{-1}\text{atom}^{-1}$.

Synthesis and Characterisation of the sample

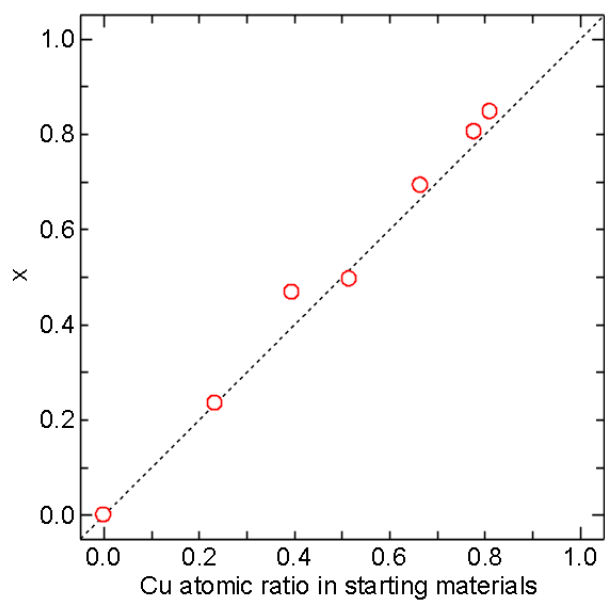


Figure S5. Content in Rh_{1-x}Cu_x nanoparticles plotted against the Cu atomic ratio in starting materials.

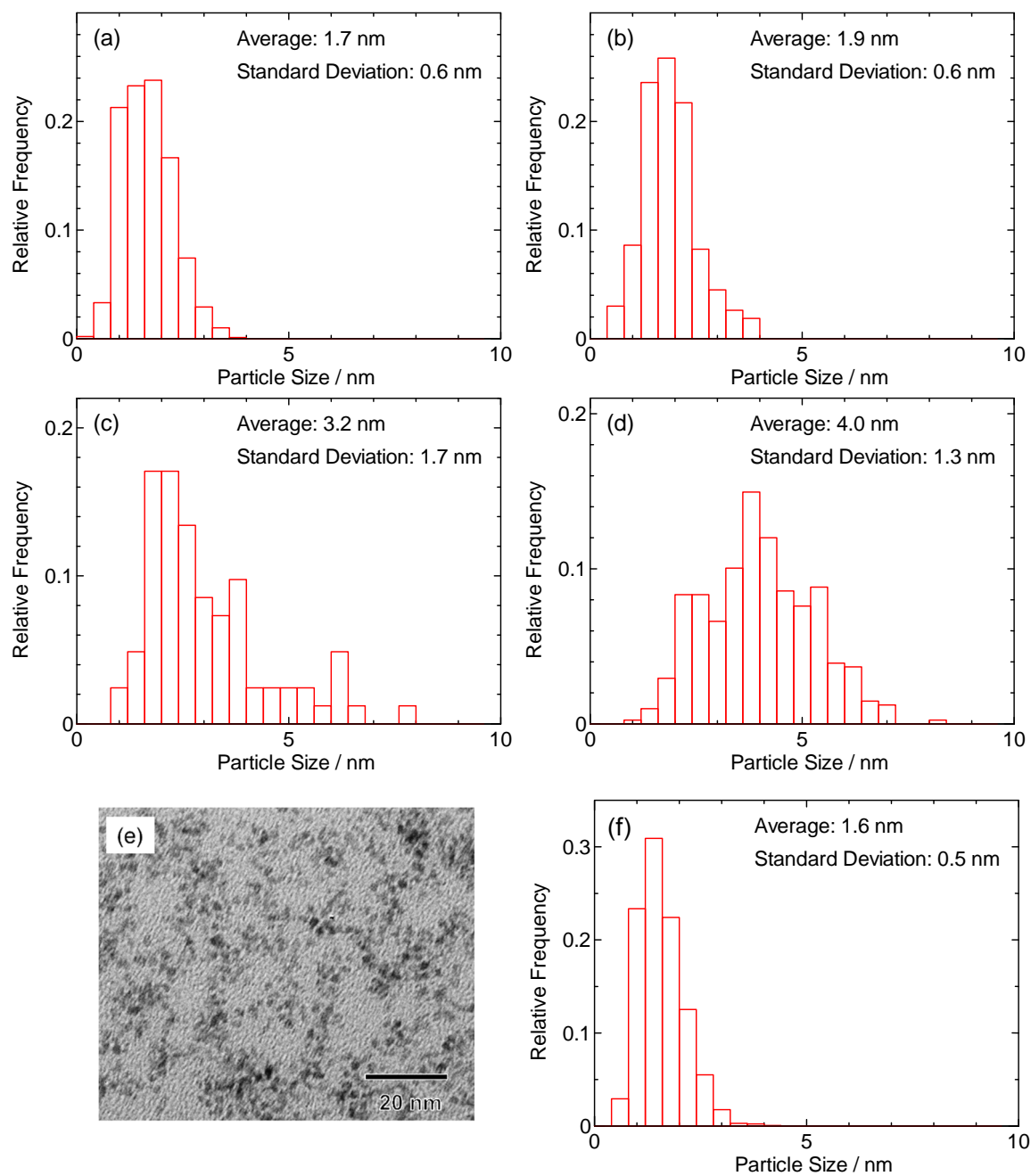


Figure S6. Size distributions obtained from TEM images of Rh_{1-x}Cu_x nanoparticles with x = 0.17 (a), 0.50 (b) 0.69 (c) and 0.81 (d). TEM image (e) and size distribution (f) of Rh nanoparticles (x=0).

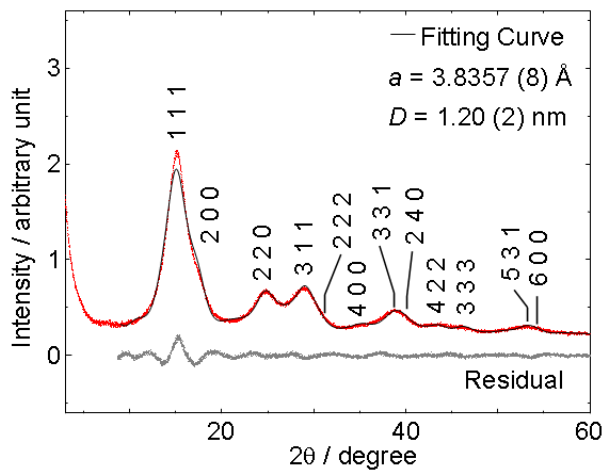


Figure S7. PXRD pattern ($\lambda = 0.58001 \text{ \AA}$) and results of Rietveld refinement for $\text{Rh}_{1-x}\text{Cu}_x$ nanoparticles with $x = 0.17$.

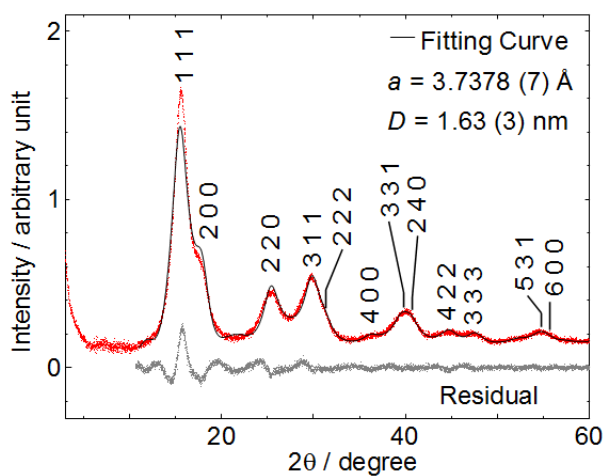


Figure S8. PXRD pattern ($\lambda = 0.58024 \text{ \AA}$) and results of Rietveld refinement for $\text{Rh}_{1-x}\text{Cu}_x$ nanoparticles with $x = 0.50$.

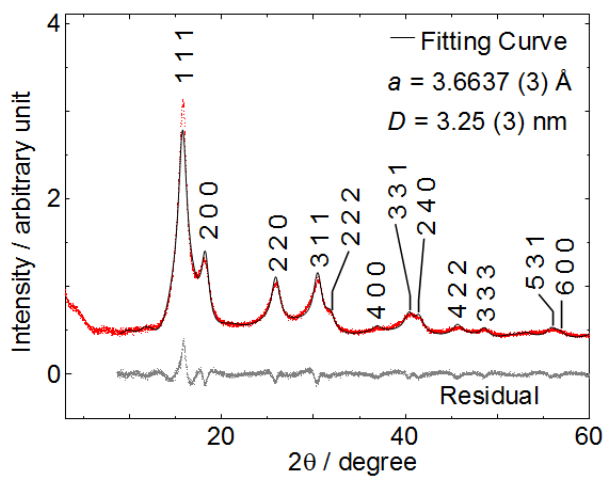


Figure S9. PXRD pattern ($\lambda = 0.58001 \text{ \AA}$) and results of Rietveld refinement for $\text{Rh}_{1-x}\text{Cu}_x$ nanoparticles with $x = 0.69$.

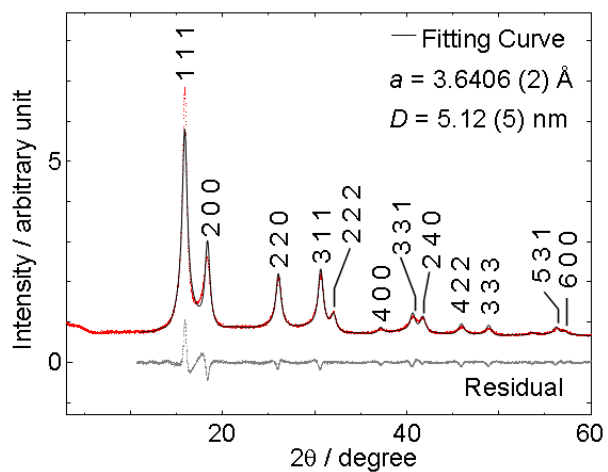


Figure S10. PXRD pattern ($\lambda = 0.58001 \text{ \AA}$) and results of Rietveld refinement for $\text{Rh}_{1-x}\text{Cu}_x$ nanoparticles with $x = 0.81$.

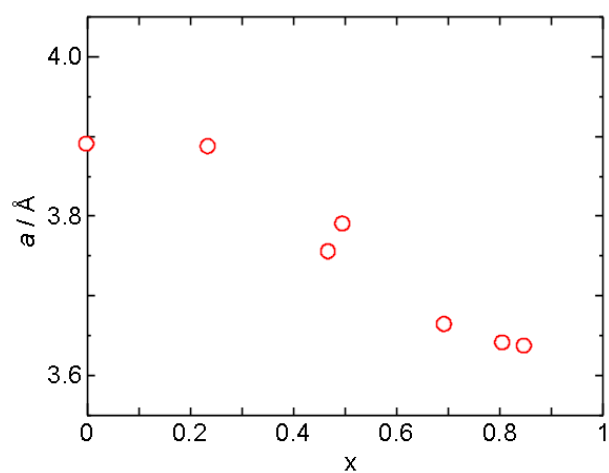


Figure S11. The lattice parameter of $\text{Rh}_{1-x}\text{Cu}_x$ nanoparticles obtained by PXRD measurements.

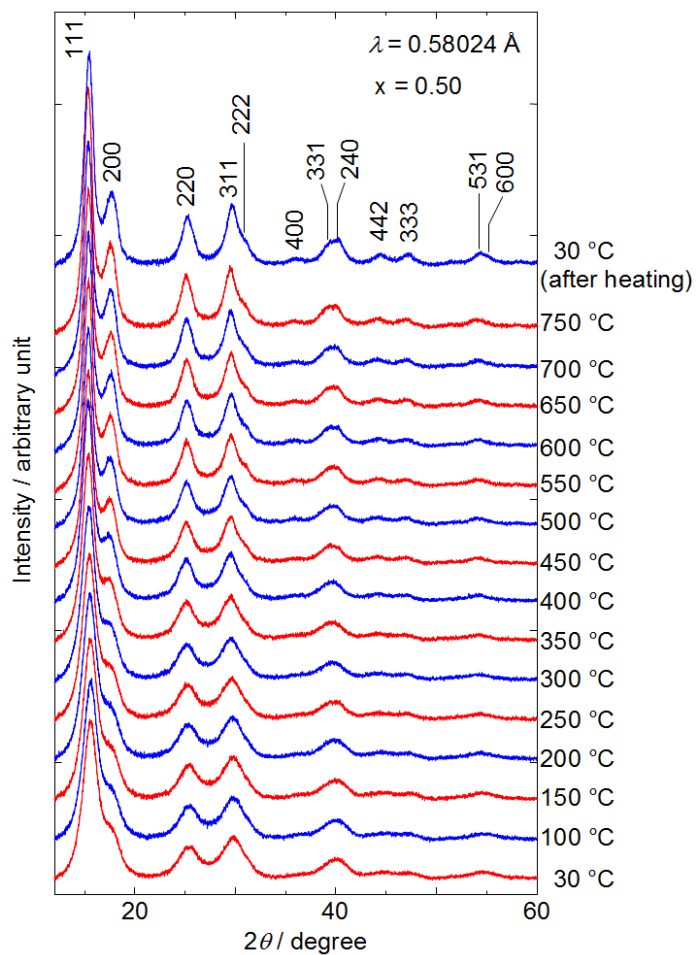


Figure S12. Powder X-ray diffraction pattern at elevated temperatures of $\text{Rh}_{1-x}\text{Cu}_x$ nanoparticles. No peak splitting due to phase separation is observed.

Catalytic activities

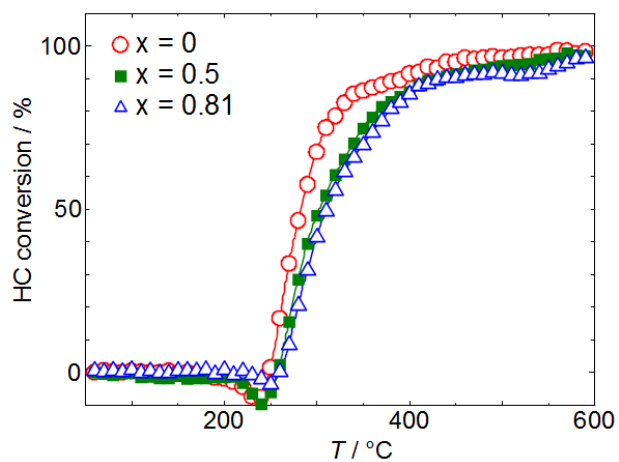


Figure S13. Temperature dependence of hydrocarbon (HC) conversion of $\text{Rh}_{1-x}\text{Cu}_x$ nanoparticles in three-way catalytic reaction.

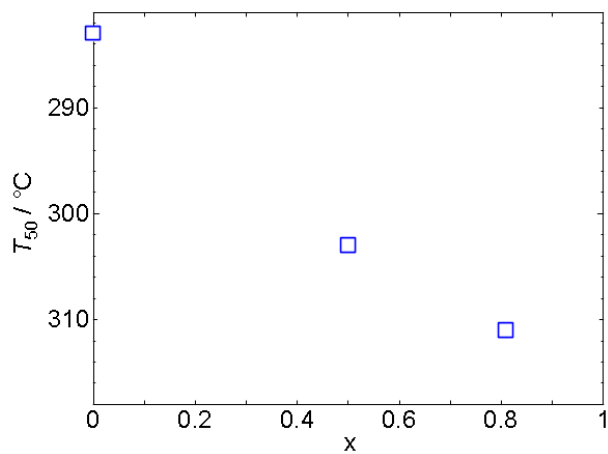


Figure S14. Catalytic activity (T_{50}) in hydrocarbon oxidation as three-way catalyst of $\text{Rh}_{1-x}\text{Cu}_x$ nanoparticles.

References

- [S1] J. P. Perdew, K. Burke, M. Ernzerhof, *Phys. Rev. Lett.* **1996**, *77*, 3865-3868.
- [S2] S. J. Clark, M. D. Segall, C. J. Pickard, P. J. Hasnip, M. J. Probert, K. Refson, M. C. Payne, *Zeitschrift fur Kristallographie* **2005**, *220*, 567-570.
- [S3] D. Vanderbilt, *Phys. Rev. B* **1990**, *41*, 7892-7895.
- [S4] H. J. Monkhorst, J. D. Pack, *Phys. Rev. B* **1976**, *13*, 5188-5192.